photonics

MDPI

Article

Wide Spectral Characteristics of Si Photonic Crystal Mach-Zehnder Modulator Fabricated by Complementary Metal-Oxide-Semiconductor Process

Yosuke Hinakura, Yosuke Terada, Takuya Tamura and Toshihiko Baba *

Department of Electrical and Computer Engineering, Yokohama National University, Yokohama 240-8501, Japan; hinakura-yosuke-zm@ynu.jp (Y.H.); yterada@ynu.ac.jp (Y.T.); tamura-takuya-nt@ynu.jp (T.T.)

* Correspondence: baba@ynu.ac.jp; Tel.: +81-045-339-4258

Received: 29 February 2016; Accepted: 29 March 2016; Published: 2 April 2016

Abstract: Optical modulators for optical interconnects require a small size, small voltage, high speed and wide working spectrum. For this purpose, we developed Si slow-light Mach-Zehnder modulators via a 180 nm complementary metal-oxide-semiconductor process. We employed 200 μm lattice-shifted photonic crystal waveguides with interleaved p-n junctions as phase shifters. The group index spectrum of slow light was almost flat at $n_g \approx 20$ but exhibited ±10% fluctuation over a wavelength bandwidth of 20 nm. The cutoff frequency measured in this bandwidth ranged from 15 to 20 GHz; thus, clear open eyes were observed in the 25 Gbps modulation. However, the fluctuation in n_g was reflected in the extinction ratio and bit-error rate. For a stable error-free operation, a 1 dB margin is necessary in the extinction ratio. In addition, we constructed a device with varied values of n_g and confirmed that the extinction ratio at this speed was enhanced by larger n_g up to 60. However, this larger n_g reduced the cutoff frequency because of increased phase mismatch between slow light and radio frequency signals. Therefore, n_g available for 25 Gbps modulation is limited to up to 40 for the current device design.

Keywords: silicon photonics; optical interconnect; photonic crystal; optical modulator; silicon modulator; Mach-Zehnder modulator

1. Introduction

The Si photonics platform enables the fabrication of dense photonic integrated circuits and reduces their production cost, thanks to the strong optical confinement of high-index-contrast Si devices and the utilization of the matured complementary metal-oxide-semiconductor (CMOS) process, respectively. It is well suited for the development of components and subsystems for optical interconnects in data centers and high-performance computers. For these cases, optical modulators are key [1–6] and a wide working spectrum and wide working temperature range are particularly required in optical interconnects, in addition to small size, low loss, low drive voltage and high speed.

Previous studies on Si modulators have mainly used a phase shift generated by carrier plasma dispersion in p-n-doped rib waveguides. Resonator-type modulators such as microring devices often show good performance with a small size, but the working spectrum is very limited and cannot operate stably without complicated thermal stabilizations [7–9]. Therefore, most studies have employed Mach-Zehnder (MZ) devices, enabling a wide working spectrum and, hence, operating over a wide temperature range without thermal stabilizations when they use a symmetric circuit. However, MZ circuits typically need a long phase shifter length of several millimeters to obtain a sufficient extinction ratio (*ER*) [1–6], resulting in high power consumption. To overcome this constraint, we have developed photonic crystal waveguide (PCW) MZ modulators. They are constructed via a CMOS process, with a phase shifter length L significantly reduced by the slow-light effect [10–15]. For

slow light with a low group velocity υ_g, the slowdown factor is usually expressed by the group index $n_g \equiv c/\upsilon_g$, where c is the light velocity in a vacuum. Values of n_g are observed to be between 3 and 4 for Si rib waveguides, while Si PCWs easily produce $n_g > 20$ [10]. In a simplified model, the phase shift $\Delta\phi$ in a waveguide with an equivalent modal index change induced by carrier plasma dispersion, Δn_{eq}, is expressed as [15,16]

$$\Delta\phi = k_0 n_g \frac{\Delta n_{eq}}{n_{eq}} \zeta L, \ \zeta \equiv \frac{n_{eq}}{\omega_b} \frac{d\omega_b}{dn_{eq}} \approx 1 \quad (1)$$

where $k_0 = 2\pi/\lambda$ is the wave number in a vacuum and ω_b is the photonic band frequency. As $\Delta\phi$ is proportional to n_g, the same value for $\Delta\phi$ can be expected even for smaller L and Δn_{eq} by employing a large n_g. Furthermore, we developed lattice-shifted PCWs (LSPCWs) that generate low-dispersion (LD) slow light, showing an almost constant n_g over the wide wavelength range of 10–20 nm for transverse-electric (TE) polarization [10]. In our recent study, we observed eye opening at some selected wavelengths and the unchanged 10 Gbps operation was confirmed for a wavelength bandwidth of 16.9 nm at wavelength $\lambda \sim 1550$ nm and a temperature range of 19–124 °C in a device with $L = 90$ μm [11]. Moreover, an interleaved p-n junction was employed, which increases the overlap of a depletion region with the slow-light mode and thus increases Δn_{eq}. This succeeded in the 25 Gbps modulation in a device with $L = 200$ μm with a drive voltage of $V_{pp} = 1.75$ V (on the panel of pulse pattern generator, PPG) [15]. In this study, we observed an *ER* of 3 dB, although the excess modulation loss (*ML*), which usually helps to increase the *ER*, was moderately suppressed to 0.8 dB.

A concern in using such LD slow light in practical modulators is the small fluctuations of n_g in a working spectrum. These fluctuations are considered to be primarily caused by the reflection at the ends of the LSPCW and may be suppressed by technical improvements. However, for the fundamental improvement of the fabrication accuracy, a more advanced CMOS process is required, which increases the production cost. It is important to estimate how severely modulation characteristics reflect fluctuations in n_g and thus modify requirements accordingly. In this study, we investigated modulation characteristics over the wide working spectrum. We measured the frequency response, *ER*, and bit-error rate (*BER*) in detail and evaluated the relation with n_g, and revealed the condition that satisfies requirements for optical interconnects.

2. Device

Figure 1a shows the schematic of the Si LSPCW MZ modulator with the interleaved p-n junction. The details of the structure, theoretical modal behaviors, and fundamental modulation characteristics can be seen in Reference [15]. Third-row-shifted LSPCWs with a central p-n junction and SiO_2 cladding as phase shifters were employed; these exhibit typical LD slow light. The phase shifter length was fixed at $L = 200$ μm and parameters of the LSPCW were a (lattice constant) = 400 nm, $2r$ (hole diameter) = 220 nm, and s (lattice shift) = 95 nm. An interleaved p-n junction with a comb period of $w_x = 300$ nm and a comb depth of $w_y = 600$ nm was used. The p- and n-type doping concentrations were given as $N_A = 9.5 \times 10^{17}$ cm^{-3} and $N_D = 5.7 \times 10^{17}$ cm^{-3}, respectively, and the p^+ and n^+ doping concentrations for electrical contacts were $N_A{}^+ = 1.0 \times 10^{19}$ cm^{-3} and $N_D{}^+ = 1.0 \times 10^{19}$ cm^{-3}, respectively. To avoid the strong free carrier absorption in heavily doped regions, a distance of ~4 μm across the p-n junction was set. As radio frequency (RF) electrodes of the phase shifters, coplanar waveguides consisting of an Al electrode for signal (S) and two Al electrodes for ground (G) were employed. No termination resistors were used, to simplify the device layout. In addition, 36.5 μm TiN heaters were integrated inside the SiO_2 cladding above the same LSPCWs, and were used for setting the initial phase of each MZ arm. The total footprint of the device excluding the input and output waveguides was ~400 × 500 μm^2, but they could be reduced to ~50 × 250 μm^2 if we shrink the electrodes and neglect the RF pads.

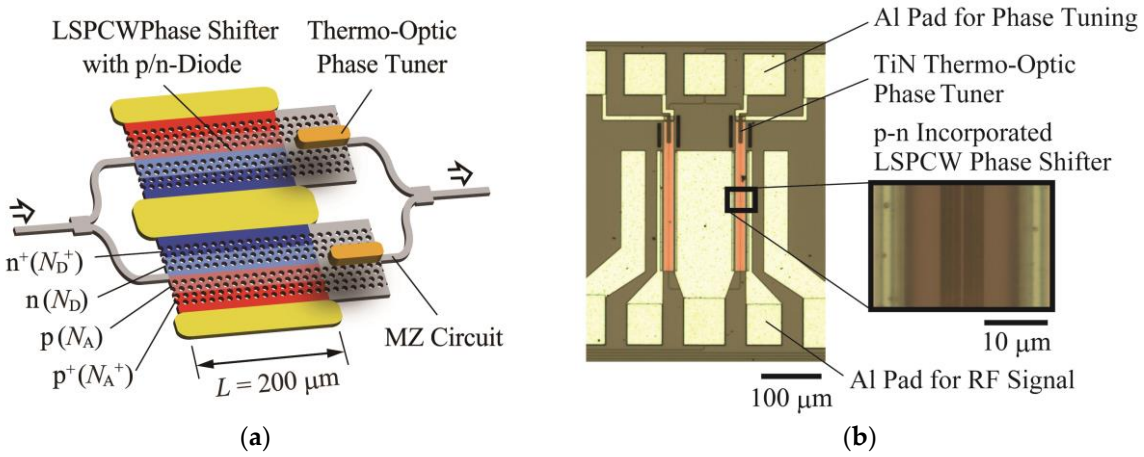

Figure 1. Si LSPCW MZ modulator. (**a**) Schematic. Interleaved p-n junction was employed but not shown in this figure; (**b**) Microscope image of fabricated device.

The devices were constructed on a 200 mm silicon-on-insulator (SOI) wafer, using a 180 nm CMOS process at the Institute of Micro-Electronics foundry service with a KrF excimer laser exposure at λ = 248 nm. The original thickness of the Si slab in the SOI wafer was 220 nm, but was subsequently thinned to 210 nm by thermal oxidation. The thickness of the SiO_2 BOX layer was 2 μm. Fourteen mask layers were used: two layers for the waveguides, four layers for the p-n junctions, two layers for the heaters and thermal isolation trench, four layers for RF and DC electrodes, contact holes, and contact pads, and two layers for the formation of waveguide end facets with spot size converters (SSC). For the waveguide layers, phase-shift masks were applied to improve the resolution to approximately 100 nm. Figure 1b shows the microscope image of the fabricated device.

First, we measured the fundamental slow-light characteristics of the device. Using objective lenses or compact lens modules, we input light from and output light to single mode fibers with the SSC consisting of SiO_2 waveguides and Si inverse tapers located at the chip facets. Figure 2a shows the transmission spectrum normalized by the transmission in a Si wire waveguide of the same length. The device exhibits a flat transmission band at λ = 1550–1570 nm with a maximum transmission of −5 dB. This excess loss came from the two 1 × 2 couplers in the MZ circuit (<0.5 dB in total), the propagation loss in the LSPCW (~3 dB), and the coupling loss between the LSPCW and Si wire (~1.5 dB in total). More than 60% of the LSPCW loss is due to the free-carrier absorption, which is expected to be reduced by optimizing the doping. Therefore, the excess loss is expected to fall by ~3 dB in future studies. Since the Si wire for the optical wiring had a 4 dB/cm propagation loss and a <0.1 dB loss at 90° bends, which corresponds to a 2 dB loss for ~4.5-mm-long wiring with six bends, the total on-chip loss of the device was 7 dB. Figure 2b shows the n_g spectrum measured by the modulation phase shift method. The device exhibited the LD band with $n_g \approx 20$ and bandwidth $\Delta\lambda \approx 20$ nm. We have reported higher n_g of 50–60 by modifying the lattice shift. However, in that case, the working spectrum was narrowed to less than 10 nm due to the constraint of the n_g-bandwidth product [10], and the strong back-scattering in the PCW, with some disordering, produced irregular oscillations. In this study, since we set n_g to be moderately low, the n_g spectrum was sufficiently wide and looks to be almost flat with no irregular oscillations. The ±10% variation of n_g observed in the n_g spectrum is considered to be due to the Fabry-Perot resonance in the LSPCW [17].

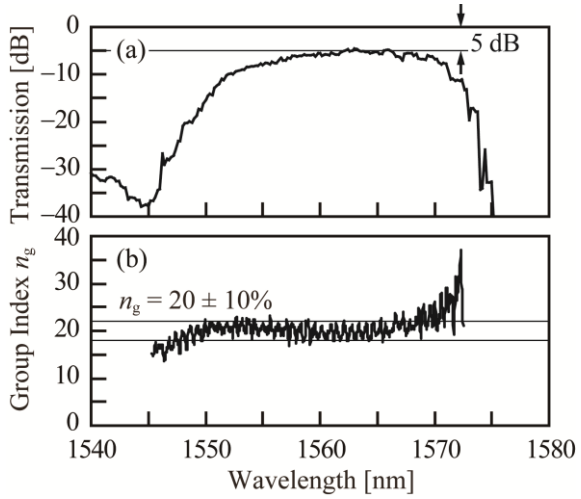

Figure 2. Slow-light characteristics of fabricated device. (**a**) Transmission spectrum; (**b**) n_g spectrum.

3. Frequency Response

The frequency response was measured using a vector network analyzer (VNA, Anritsu 37269E-R, Atsugi, Japan). Small sinusoidal signals from the VNA were applied to the RF electrode of a single MZ arm through an RF probe (typical insertion loss is 0.8 dB), and the modulated signals were then returned to the VNA through an erbium-doped fiber amplifier (EDFA, Alnair Labs CPA-100-CL, Shinagawa, Japan), a band-pass filter (BPF, Alnair Labs CVF-220-CL, Shinagawa, Japan) and an opto-electronic (OE) converter (Anritsu MN4765, Atsugi, Japan). Figure 3 shows S_{11} for the RF signals reflected to the output port of the VNA and S_{21} for the modulated optical signals that were input into the VNA. As previously mentioned, the device did not have termination resistors, and thus S_{11} becomes 0 dB at low frequencies. At high frequencies, on the other hand, the RF signals tend to attenuate during the transmission due to the parasitic resistance at the p-n junction, which decreases S_{11} gradually. The dip appearing at 19 GHz is considered to be caused by the excitation of the coupled slotline mode. This will be suppressed by symmetrizing the GSG RF electrode, which was designed asymmetrically in this fabrication, and the connection between the two G electrodes [4,18]. In any case, the reflection of the RF signals generates a voltage on the electrode two times greater than the set value at the PPG at low frequencies, 1.7 times greater at 12 GHz exhibiting $S_{11} = -3$ dB, and 1.4–1.5 times greater at 15 GHz exhibiting $S_{11} = -6$ dB. This enhances the total modulation efficiency while relatively degrading the high-frequency response.

For the electro-optic (EO) S_{21} measurement, a TE-polarized laser light at $\lambda = 1554$ nm was coupled to the SSC through a polarization-maintaining single mode fiber with a lens module. The coupling loss was 3.5 dB, including a 1 dB loss inside the lens module (7 dB in total for the input and output). The total insertion loss from fiber to fiber was approximately 14 dB including a 7 dB on-chip loss. Furthermore, the total loss from the laser source to the output fiber was 21 dB, including losses at the polarization controller and some junctions between fibers. Therefore, the laser power was raised to 16.5 dBm and S_{21} was measured. The cutoff frequency f_{3dB} was 17 GHz, which is sufficient for the 25 Gbps operation. In general, f_{3dB} is constrained by the RC time constant. We have reported the calculation of the resistance R and capacitance C at the p-n junction using the commercial simulator Lumerical DEVICE in Reference [15]. Modeling the Si layer sandwiched by the SiO_2 BOX layer and top SiO_2 cladding (both insulators), they were calculated to be 96 Ω (146 Ω including 50 Ω internal resistance in the PPG connected in series with the R) and ~60 fF at $V_b = -2.2 \times 2$ V, respectively, for the current design. Their product gives $f_{3dB} = 18$ GHz, which almost agrees with the measured value.

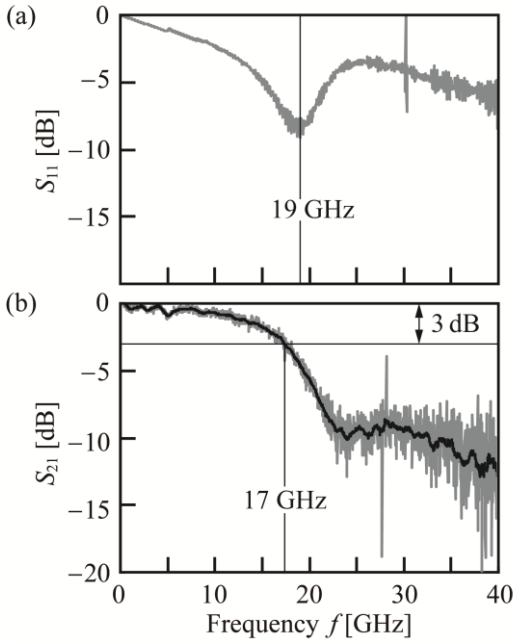

Figure 3. Measured S parameters: (**a**) S_{11}; (**b**) EO S_{21} at λ = 1554 nm. Gray line shows raw data. Black line shows averaged values within each ~0.5 GHz range.

The f_{3dB} could be constrained by the phase mismatch between the slow light and RF signals. The decreased ratio of the modulation depth, η(f), is expressed as

$$\eta(f) = \frac{1}{L}\int_0^L \cos\left\{\left(n_g - n_{RF}\right)\frac{2\pi f z}{c} + \theta_0\right\} dz \quad (2)$$

where n_{RF} is the refractive index for RF signals, c is the light velocity in a vacuum, and θ_0 is the initial phase mismatch. EO S_{21} is expressed using electro-electronic (EE) S_{21} for RF signals as

$$\text{EO}\,S_{21} = \eta(f) \cdot \text{EE}\,S_{21} \quad (3)$$

For typical traveling-wave modulators, a small phase mismatch is compensated by optimizing the design. In slow-light modulators, on the other hand, this issue is more complicated due to the large differences between group velocities. Let us assume that f = 12.5 GHz is a critical frequency for 25 Gbps modulation. Then, for n_g = 20, n_{RF} = 2 and L = 200 μm, η(f) is calculated to be higher than 0.95 when θ_0 is optimized. Thus, the phase mismatch issue is not so severe. However, if either n_g, L or f is larger than their present values, it will become a limiting factor to the frequency response; η(f) will be less than 0.9 when $n_g \geqslant 32$, $L \geqslant 340$ μm or $f \geqslant 22$ GHz.

We measured the frequency response spectrum $R(f, \lambda)$ by changing λ in steps of 0.02 nm in the LD band within the range λ = 1550–1558 nm. Figure 4 shows the measured results as a color plot, as well as the measured n_g spectrum and calculated f_{3dB} spectrum from Equations (2) and (3). $R(f, \lambda)$ exhibits fluctuations, which are considered to reflect the n_g spectrum, although they do not agree completely. The n_g spectrum shows a relatively large and slow oscillation with an averaged period of 0.7 nm, and a small and fast oscillation with an averaged period smaller than 0.2 nm. This large and slow oscillation roughly corresponds to the fluctuations in $R(f, \lambda)$ at f > 20 GHz, and therefore may correspond to the effect of the phase mismatch at higher f. On the other hand, f_{3dB} depicted by the boundary between red and yellow regions only exhibits the small and fast fluctuation, lying between 15 and 20 GHz, with the exception of three wavelengths that show f_{3dB} = 12–13 GHz. Thus, the frequency response of this device satisfies the requirement for the 25 Gbps operation over the wide wavelength range.

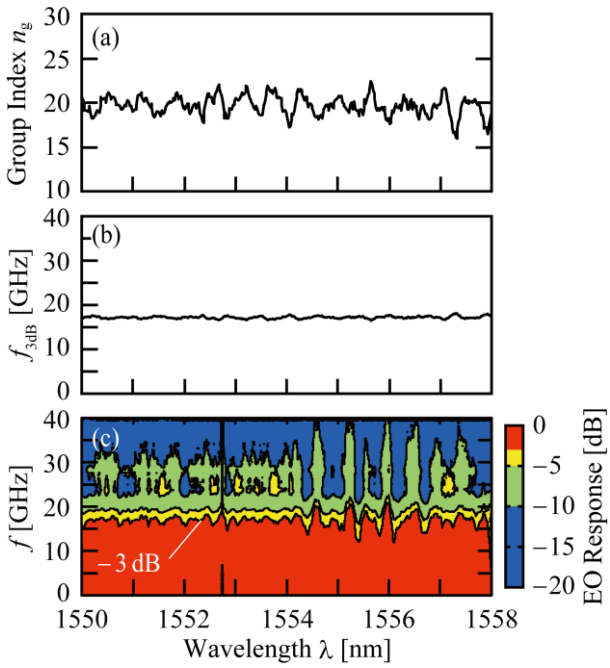

Figure 4. Fluctuations in frequency response over the wide wavelength range: (**a**) n_g spectrum; (**b**) f_{3dB} spectrum calculated from Equations (2) and (3) with the measured n_g and EE S_{21} estimated with R = 96 Ω and C = 50 fF; (**c**) Frequency response spectrum $R(f, \lambda)$ obtained from the averaged response at each λ, such as those represented by the black line in Figure 3b. The f_{3dB} is shown by the boundary between red and yellow regions. The fluctuation in the measurement setup was smaller than 1 GHz.

4. Signal Modulation

The 25 Gbps signal modulation was investigated over the wide wavelength range, using the non-return-to-zero (NRZ) pseudo-random-bit sequence (PRBS). Although the voltages from PPG (Anritsu MP1800A, Atsugi, Japan) were set as $V_b \approx -1$ V and V_{pp} = 2.0 V, actual applied voltages should be modified by the open-ended electrodes, as mentioned above. The operation was first measured at λ = 1561 nm. Since the device and measurement setup had losses as outlined above, the output light from the device was amplified using EDFA and BPF, and then received and analyzed by an optical sampling oscilloscope (Keysight 86100C, 86109A, Santa Rosa, CA, USA). Figure 5a shows the eye pattern when the initial phase of the MZ arms was adjusted so that $ER \approx 3$ dB was obtained. The open eye was observed with ML = 0.5 dB, which is comparable to that in a previous study [15]. Figure 5b shows a clearer open eye with ER = 3.9 dB when the ML was slightly increased to 1 dB.

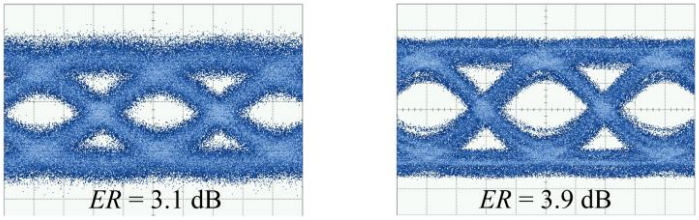

(**a**) (**b**)

Figure 5. The 25 Gbps eye patterns of modulated light: (**a**) ML = 0.5 dB and (**b**) 1.0 dB with PRBS lengths of $2^{31} - 1$ and $2^7 - 1$, respectively.

Next, *ER* was repeatedly measured, changing the wavelength in steps of 0.5 nm between the range λ = 1549.5–1565.5 nm. The initial phase was adjusted such that the output intensity with no V_{pp} was decreased to 2 dB lower than the maximum, thus giving $ML = 2 - ER/2$. This is almost the same condition as that in Figure 5. Figure 6 shows the spectra of *ER* and n_g. Although they do not agree completely, they exhibit similar patterns. *ER* ranges between 2 and 3 dB and fluctuates by ~1 dB. Furthermore, *ER* and *BER* were measured, within the range λ = 1558–1560 nm in steps of 0.2 nm. For the *BER* measurement, amplified light was detected by an OE converter (Agilent 11982A) after passing through a variable optical attenuator, where the electrical signal was incident on an error detector module (Anritsu MU183040B) after removing the DC components. Voltages from the PPG and initial phase were set similarly to those presented in Figure 6. Figure 7a shows *BER* measured as a function of the received powers P_r at the OE converter. The error-free operation of $BER < 10^{-11}$ was confirmed. Figure 7 compares the *BER* and *ER* spectra measured in steps of 0.2 nm in the range of λ = 1558–1560 nm. *ER* fluctuated by 1 dB, similarly to that in Figure 6. In other words, the *BER* finally reflects the fluctuations in n_g through those in the *ER*. This indicates that a margin larger than 1 dB is necessary in *ER* for a stable, error-free operation. For optical interconnects, *ER* is required to be larger than 3 dB, although it depends on the specifications of the transmitter and receiver. However, for the modulator described in this study, *ER* should be greater than 4 dB, including the margin. This is achieved by increasing the *ML* by 0.5 dB and the loss is compensated by increasing the output power from the light source or reducing the passive losses.

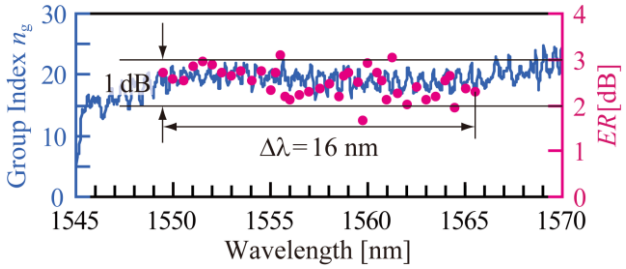

Figure 6. Spectra of n_g and *ER* measured at 25 Gbps. Operating condition was similar to that for Figure 5.

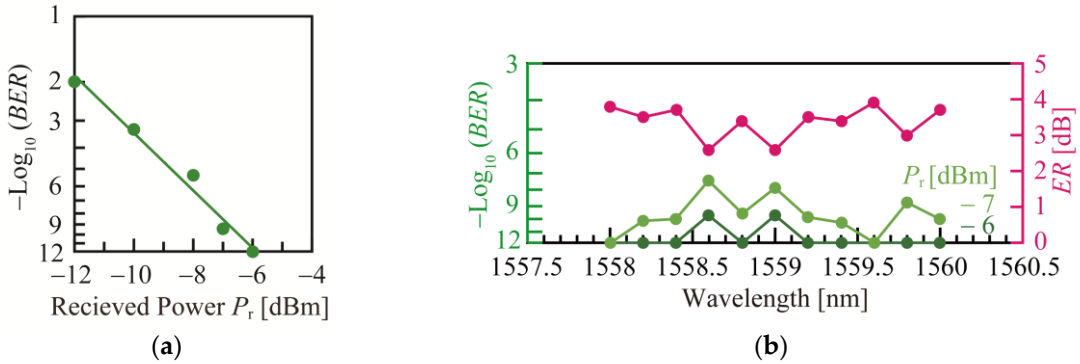

Figure 7. *BER* characteristics at 25 Gbps for $2^7 - 1$ bit NRZ-PRBS signals: (**a**) *BER* at λ = 1559.6 nm; (**b**) *BER* and *ER* at λ = 1558–1560 nm.

5. Slow-Light Enhancement

Thus far, the modulation characteristics have been presented with a fixed $n_g \approx 20$. In this section, the characteristics for a varied n_g are presented. For a SiO_2-cladded PCW, without a lattice shift, n_g increases as λ increases towards the photonic band edge. Since this increase is smaller than that in air-bridge structures which have been extensively studied in the past, this allows for a wide scan

of n_g and the comprehensive investigation of the slow-light enhancement, by only changing λ. Here, the PCW was designed with specifications of a = 400 nm, $2r$ = 200 nm, and s = 0 nm. Due to different fabrication lots, doping concentrations were lower than those given above, *i.e.*, $N_A = 4.8 \times 10^{17}$ cm^{-3} and $N_D = 4.8 \times 10^{17}$ cm^{-3}, and the p-n junction profile was linear. Therefore, the modulation efficiency should be lower than that in the device described in the previous sections. The absolute value of the efficiency was neglected, while focusing on the relative change of the modulation characteristics with n_g.

Figure 8 presents the measured n_g spectrum, with the f_{3dB} spectrum calculated in the same way as that for Figure 4b, and measured $R(f, \lambda)$ at λ = 1534–1540 nm. It is shown that n_g changes widely from 20 to 60 within this range. The calculated f_{3dB} decreases with the increasing n_g, showing the influence of the phase mismatch. The f_{3dB} estimated from the measured $R(f, \lambda)$ was 10–20 GHz at $n_g \approx 20$, but then fell to less than 10 GHz for higher n_g, which almost agrees with the calculated one. Thus, some solution to suppress the phase mismatch is necessary when n_g is increased to enhance $\Delta\phi$. Solutions need to slow down the RF signals and/or to shift back the phase of the RF signals inside the electrode. For the former, a slow-wave electrode consisting of a loaded transmission line has previously been studied [6,19–22]. However, their slow-down factors are too small to compensate the phase mismatch. For the latter, it is possible to add a delay line, such as a meander line; however, this will increase the device footprint as its length will be in the order of millimeters. Furthermore, the fluctuations in f_{3dB} in Figure 8 become particularly large at $n_g > 40$, possibly caused by the oscillation of n_g. As previously mentioned, a large n_g generates strong back-scattering and, in particular, enlarges the spectral oscillation. A more advanced CMOS process is necessary to completely improve this situation, which may be costly. Alternatively, n_g can be set to no higher than 40 if the current CMOS process is used, with the application of the slow light to the modulator.

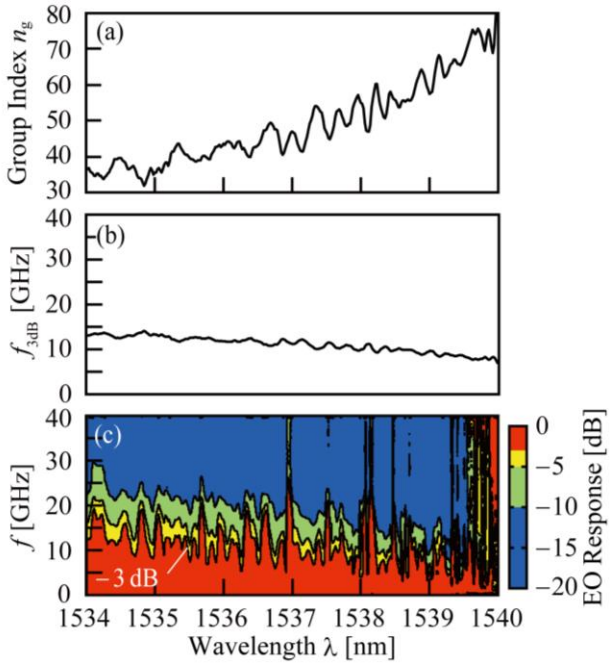

Figure 8. Characteristics of PCW device without lattice shifts in the wide wavelength range: (**a**) n_g spectrum; (**b**) f_{3dB} spectrum calculated from Equations (2) and (3) with the measured n_g and EE S_{21} estimated with R = 96 Ω and C = 50 fF; (**c**) Frequency response spectrum $R(f, \lambda)$.

Figure 9 shows the result of the signal modulations. Although the voltages are the same as for Figure 5, the initial phase was set such that the transmission with no V_{pp} was reduced to 9 dB lower than the maximum, resulting in a large ML, and, hence, compensating for the low modulation

efficiency. The *ER* was 2.5 dB at n_g = 25, but increased to 8.1 dB at n_g = 64. Figure 10 shows $\Delta\phi$ estimated from the *ER* as a function of n_g. As expected from Equation (1), $\Delta\phi$ is almost proportional to n_g, and therefore confirms the slow-light enhancement in the modulation efficiency. Equation (1) also indicates that $\Delta\phi$ depends on Δn_{eq}, which is determined by the overlap between the guided mode and the depletion region of the p-n junction. If the distribution of the slow-light mode changes with n_g, Δn_{eq} would also change. Inversely speaking, the proportional behaviors between $\Delta\phi$ and n_g suggest that the distribution is almost unchanged or is less severe for the modulator performance in this range. Equations (2) and (3) and the results in Figure 8 also suggest that such large n_g makes the phase mismatch more severe and decreases $\Delta\phi$. However, it is not apparent in Figure 10 because the slow-light enhancement in Equation (1) might be more dominant for the 25 Gbps PRBS signals whose major frequency components are lying at <12.5 GHz.

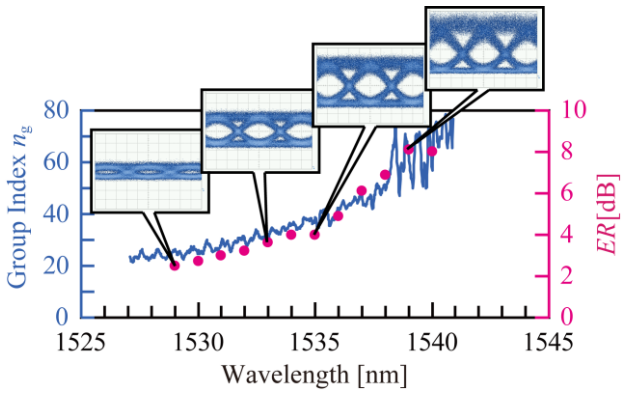

Figure 9. The n_g spectrum of PCW device without lattice shifts and *ER* at 25 Gbps modulation. Set voltages were the same as those for Figure 5.

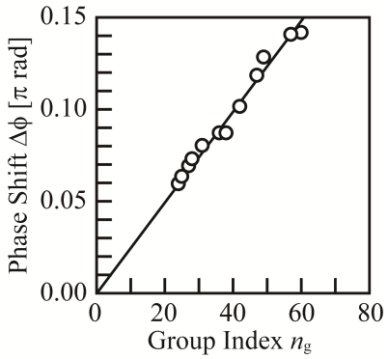

Figure 10. The $\Delta\phi$ estimated from *ER* as a function of n_g.

6. Conclusions

Si lattice-shifted photonic crystal slow-light modulators were constructed using a 180 nm CMOS process, with a phase shifter length as short as 200 μm. The frequency response, *ER*, and *BER* were measured in wide wavelength ranges, with fluctuations observed, perhaps due to the oscillation in the group index n_g spectrum. The device with $n_g \approx 20$ showed a wide working spectrum of 20 nm and a sufficient frequency response for the 25 Gbps modulation. A higher n_g up to 60 is available by modifying the lattice shift but the working spectrum is comparably narrowed, which is the major constraint of the slow-light effect. Even for the moderately low $n_g \approx 20$, the $\pm$10% fluctuation was observed in the n_g spectrum, which was reflected in *ER* and *BER*. Therefore, a margin larger than 1 dB is necessary in *ER* for stable, error-free operation, which can be achieved by adding a 0.5 dB modulation loss, comparably increasing the light source power and/or reducing passive losses. The *ER*

was simply increased by increasing n_g; however, the frequency response was degraded simultaneously. This degradation was considered to be due to the phase mismatch between slow light and RF signals, which will be more problematic beyond 25 Gbps. Results suggest that n_g should be set to less than 40 to avoid this degradation and avoid irregularly large oscillations in *ER*, which is particularly enhanced by slow light.

Acknowledgments: This work was partly supported by the New Energy and Industrial Technology Development Organization (NEDO), Japan.

Author Contributions: Yosuke Hinakura, Yosuke Terada and Toshihiko Baba conceived and designed the experiments; Yosuke Terada, Takuya Tamura and Toshihiko Baba designed the devices; Yosuke Hinakura and Yosuke Terada performed the experiments; Yosuke Hinakura analyzed the data; Toshihiko Baba contributed experiment systems, analysis tools; Yosuke Hinakura and Toshihiko Baba wrote the paper.

Conflicts of Interest: The authors declare no conflict of interest.

References

1. Reed, G.T.; Mashanovich, G.; Gardes, F.Y.; Thomson, D.J. Silicon optical modulators. *Nat. Photonics* **2010**, *4*, 518–526. [CrossRef]
2. Thomson, D.J.; Gardes, F.Y.; Fedeli, J.M.; Zlatanovic, S.; Hu, Y.; Kuo, B.P.P.; Myslivets, E.; Alic, N.; Radic, S.; Mashanovich, G.Z.; *et al*. 50-Gb/s silicon optical modulator. *IEEE Photonics Technol. Lett.* **2012**, *24*, 234–236. [CrossRef]
3. Yang, L.; Ding, J. High-speed silicon Mach-Zehnder optical modulator with large optical bandwidth. *J. Lightwave Technol.* **2014**, *32*, 966–970. [CrossRef]
4. Xu, H.; Li, X.; Xiao, X.; Li, Z.; Yu, Y.; Yu, J. Demonstration and characterization of high-speed silicon depletion-mode Mach-Zehnder modulators. *IEEE J. Sel. Top. Quantum Electron.* **2014**, *20*, 23–32. [CrossRef]
5. Akiyama, S.; Imai, M.; Baba, T.; Akagawa, T.; Hirayama, N.; Noguchi, Y.; Seki, M.; Koshino, K.; Toyama, M.; Horikawa, T.; *et al*. Compact PIN-diode-based silicon modulator using side-wall-grating waveguide. *IEEE J. Sel. Top. Quantum Electron.* **2013**, *19*, 74–84. [CrossRef]
6. Ding, R.; Liu, Y.; Ma, Y.; Yang, Y.; Li, Q.; Lim, A.E.J.; Lo, G.Q.; Bergman, K.; Baehr-Jones, T.; Hochberg, M. High-speed silicon modulator with slow-wave electrodes and fully independent differential drive. *J. Lightwave Technol.* **2014**, *32*, 2240–2247. [CrossRef]
7. Timurdogan, E.; Sorace-Agaskar, C.M.; Sun, J.; Hosseini, E.S.; Biberman, A.; Watts, M.R. An ultralow power athermal silicon modulator. *Nat. Commun.* **2014**, *5*, 4008. [CrossRef] [PubMed]
8. Zheng, X.; Chang, E.; Amberg, P.; Shubin, I.; Lexau, J.; Liu, F.; Thacker, H.; Djordjevic, S.S.; Lin, S.; Luo, Y.; *et al*. A high-speed, tunable silicon Photonic ring modulator integrated with ultra-efficient active wavelength control. *Opt. Express* **2014**, *22*, 12628–12633. [CrossRef] [PubMed]
9. Sun, C.; Wade, M.T.; Lee, Y.; Orcutt, J.S.; Alloatti, L.; Georgas, M.S.; Waterman, A.S.; Shainline, J.M.; Avizienis, R.R.; Lin, S.; *et al*. Single-chip microprocessor that communicates directly using light. *Nature* **2015**, *528*, 534–538. [CrossRef] [PubMed]
10. Tamura, T.; Kondo, K.; Terada, Y.; Hinakura, Y.; Ishikura, N.; Baba, T. Silica-Clad Silicon Photonic Crystal Waveguides for Wideband Dispersion-Free Slow Light. *J. Lightwave Technol.* **2015**, *33*, 3034–3040. [CrossRef]
11. Nguyen, H.C.; Sakai, Y.; Shinkawa, M.; Ishikura, N.; Baba, T. 10 Gb/s operation of photonic crystal silicon optical modulators. *Opt. Express* **2011**, *19*, 13000–13007. [CrossRef] [PubMed]
12. Nguyen, H.C.; Sakai, Y.; Shinkawa, M.; Ishikura, N.; Baba, T. Photonic crystal silicon optical modulators: Carrier-injection and depletion at 10 Gb/s. *IEEE J. Quantum Electron.* **2012**, *48*, 210–220. [CrossRef]
13. Nguyen, H.C.; Hashimoto, S.; Shinkawa, M.; Baba, T. Compact and fast photonic crystal silicon optical modulators. *Opt. Express* **2012**, *20*, 22465–22474. [CrossRef] [PubMed]
14. Nguyen, H.C.; Yazawa, N.; Hashimoto, S.; Otsuka, S.; Baba, T. Sub-100 μm photonic crystal Si optical modulators: Spectral, athermal, and high-speed performance. *IEEE J. Sel. Top Quantum Electron.* **2013**, *19*, 127–137. [CrossRef]
15. Terada, Y.; Ito, H.; Nguyen, H.C.; Baba, T. Theoretical and experimental investigation of low-voltage and low-loss 25-Gbps Si photonic crystal slow light Mach-Zehnder modulators with interleaved p/n junction. *Front. Phys.* **2014**, *2*, 1–9. [CrossRef]

16. Brosi, J.M.; Koos, C.; Andreani, L.C.; Waldow, M.; Leuthold, J.; Freude, W. High-speed low-voltage electro-optic modulator with a polymer-infiltrated silicon photonic crystal waveguide. *Opt. Express* **2008**, *16*, 4177–4191. [CrossRef] [PubMed]
17. O'Faolain, L.; Schulz, S.A.; Beggs, D.M.; White, T.P.; Spasenović, M.; Kuipers, L.; Morichetti, F.; Melloni, A.; Mazoyer, S.; Hugonin, J.P.; *et al*. Loss engineered slow light waveguides. *Opt. Express* **2010**, *18*, 27627–27638. [CrossRef] [PubMed]
18. Ponchak, G.E.; Papapolymerou, J.; Tentzeris, M.M. Excitation of coupled slotline mode in finite-ground CPW with unequal ground-plane widths. *IEEE Trans. Microwave Theory Technol.* **2005**, *53*, 713–717. [CrossRef]
19. Shin, J.H.; Sakamoto, S.R.; Dagli, N. Conductor loss of capacitively loaded slow wave electrodes for high-speed photonic devices. *J. Lightwave Technol.* **2011**, *29*, 48–52. [CrossRef]
20. Chen, H.W.; Kuo, Y.H.; Bowers, J.E. 25 Gb/s hybrid silicon switch using a capacitively loaded traveling wave electrode. *Opt. Express* **2010**, *18*, 1070–1075. [CrossRef] [PubMed]
21. Li, G.L.; Mason, T.G.B.; Yu, P.K.L. Analysis of segmented traveling-wave optical modulators. *J. Lightwave Technol.* **2004**, *22*, 1789–1796. [CrossRef]
22. Jaeger, N.A.; Lee, Z.K. Slow-wave electrode for use in compound semiconductor electrooptic modulators. *IEEE J. Quantum Electron.* **1992**, *28*, 1778–1784. [CrossRef]